To cite this version :

Wenjing ZHANG, Ngac Ky NGUYEN, Eric SEMAIL, Yanliang XU - Axial Stress Analysis and Comparison of the Novel Dual 3-phase Axial Flux Permanent Magnet Machines - In: 2023 11th International Conference on Power Electronics and ECCE Asia (ICPE 2023 - ECCE Asia), Corée du sud, 2023-05-22 - 2023 11th International Conference on Power Electronics and ECCE Asia (ICPE 2023 - ECCE Asia) - 2023

Axial Stress Analysis and Comparison of the Novel Dual 3-phase Axial Flux Permanent Magnet Machines

Wenjing Zhang[1], Ngac Ky Nguyen[2], Eric Semail[2], Yanliang Xu[1]

[1] School of Electrical Engineering, Shandong University, China

[2] Laboratory of Electrical Engineering and Power Electronics, University of Lille, Arts et Metiers Institute of Technology, Centrale Lille, Yncrea Hauts-de-France, ULR 2697-L2EP, France

Abstract-- **In previous research, a novel three-phase dual-stator axial flux permanent magnet machine characterized by the advantages of compact structure and low moment of inertia is proposed for industrial robot application. In order to improve its functional reliability furtherly, the dual three-phase axial flux permanent magnet machine (DTP-AFPM) is firstly proposed. Benefiting from the combination of 12 slots/ 10 poles, the coil configuration of one stator disk can be modified to a dual three phase full-pitch winding straightforwardly, as a result, one kind of the DTP-AFPMs is achieved which is named as the no shift model in this paper. For eliminating the coil reconfiguration on each stator disk and the connection of the coils belonging to the same phase between two stator disks, the shift model which is based on the shift of the two stator disks to obtain the phasor difference between two three-phase windings is introduced. The characteristics and electromagnetic performances of these two models are analyzed and compared. However, it should be noted that the light-weight disk-type rotor of DTP-AFPMs also degrade the strength of the rotor. The proposed DTP-AFPMs are more sensitive to the axial stress on the rotor which introduces not only the vibration and noise but also the deformation or even the damage of the rotor. Thus, the axial stress on the rotor is investigated and treated as a critical evaluation indicator. The axial stress is analyzed under both healthy and fault conditions and its distribution on the rotor is given on a 2-D plane.**

Index Terms-- **Axial flux permanent magnet machine, dual three-phase, one-phase-open, fault tolerant control, axial stress.**

I. INTRODUCTION

In previous research[1], a novel axial flux permanent magnet machine (AFPM) as shown in Fig. 1 is proposed for the industrial robot application where the low volume, low moment of inertia and additional space for kinds of accessories are required.

Normally, the 3-phase machine is enough for most industry applications. However, due to its unsatisfactory presentation on reliability, the demands for the multiphase machine has been growing. Besides the superiority in reliability [2][3], the multiphase machine also combines the advantages of low voltage rating [4], high power density [5] and high torque density by injecting harmonics [6]. In [7], a seven-phase axial flux permanent magnet machine supplied by a seven-leg voltage source inverter is proposed, the machine is able to work easily with one or two open-circuited phases by means of two supplementary degrees of freedom for fault mode configuration. In [8], the authors analyze a nine-phase surface-mounted PMSM, the output torque is improved by using non-sinusoidal back EMF and the sensor fault can be solved based on the harmonic components in EMF. In [9] and [10], the authors both develop multiphase permanent magnet machine for aircraft application considering the strict requirement for the safety of the flight which can be improved by the fault-tolerant capability of multiphase winding structure.
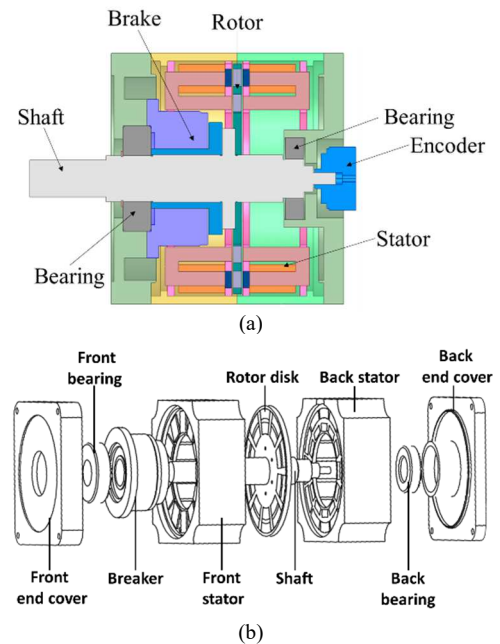

Fig. 1. Topology of the proposed novel AFPM in [1]: (a) Section view (b) Explosive view.

Dual 3-phase machine is one of the widely applied form which combines the advantages of control easily for conventional 3-phase machine and fault-tolerant capability for multiphase machine. Besides, the proposed novel AFPM is more suitable to be transformed to a dual 3-phase machine due to its winding configuration and dual-sides stator structure [1].

The AFPM benefits from the advantages of compact structure [11] and high torque density [12]. However, the

AFPMs is generally characterized by a disk-type rotor of which the strength is relatively lower compared with the radial flux rotor. Thus, the analysis of the axial stress on the rotor is important. According to the Maxwell stress tensor theory, there are three types of stress exerted on the rotors of the AFPM: tangential stress which is the origin of the output torque, radial stress and axial stress that are the results of the vibration and acoustic noise. And it is proved that the magnitude of the radial stress in AFPM is much lower compared with the axial stress and can be neglected as illustrated in [13]. In terms of the single-side AFPM, the axial force on rotor is dangerously high. And the uneven axial force distribution on the surface of the rotor also deteriorate the problems of vibration and noise [14]. To deal with this problem, the double-stator single-rotor symmetric topology is adopted of which the axial force on the rotor can be balanced. However, the balance will be destroyed while there is an asymmetrical condition either in mechanical structure or the winding distribution and it is bound to deteriorate furtherly while the AFPM are working under the post-fault condition [15]. For the proposed structure in [1] which adopt a coreless light-weight rotor, this problem is more significant. As a result, the axial stress on the rotor is a vital indicator to evaluate the feasibility of the proposed novel structure.

In this paper, the transformation from a previously proposed 3-phase AFPM to two kinds of dual 3-phase axial flux permanent magnet machines (DTP-AFPM) is introduced firstly. The electromagnetic performances are analyzed. In section III, the control method under both healthy and fault conditions are presented briefly. One phase open-circuit fault is considered and the fault tolerant control (FTC) strategy is adopted. The simulation results are given and the phase current is used to calculate the axial stress. In section IV, the axial stress distribution on the rotor is analyzed and compared between the two DTP-AFPM models in three different stages.

II. STRUCTURE AND ELECTROMAGNETIC ANALYSIS

A. Structure and Coil Configuration of DTP-AFPMs

The structure of 3-phase AFPM that has been researched in previous work is shown in Fig. 2. The double-stator single rotor topology is adopted of which the two stator disks are symmetrically arranged at the two sides of the rotor disk as shown in Fig. 2(a). Each stator disk is composed of 12 segmented armatures. As shown in Fig. 2(b), the segmented armature consists of a stator shoe made by SMC material, stator body made by Si-steel and the coil. The commonly used coil configuration W1 for 10 poles/12 slots machine as shown in Fig. 3(a) is used by which a short-pitch concentrated winding is obtained. The coil configurations of both two stator disks are identical. The phasor arrangement of the two stator disks is shown in Fig. 4(a). All coils of two stator disks belong to the identical phase are connected serially.

Based on the 10 poles/12 slots combination of 3-phase AFPM, it is convenient to turn it into a novel DTP-AFPM which benefits from some additional advantages such as fault-tolerance capability, lower voltage-level and lower torque ripple. A dual 3-phase full-pitch concentrated

winding is achieved by modifying the coil configuration in accordance with W2 as given in Fig. 3(b). It can be noticed that the phasor difference of two winding sets is 30 electrical degrees which eliminates the 6th harmonics in torque ripple. The phasor arrangement of the two stator disks is shown in Fig. 4(b). The coils of the identical phase sequence are connected serially.
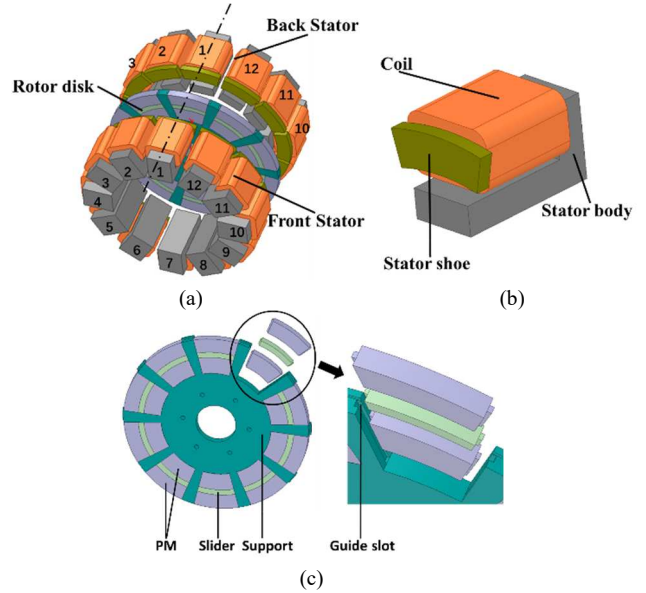

Fig. 2. Structure of previous 3-phase DTFPM: (a) Total structure (b) Single armature stator core (c) Rotor part.
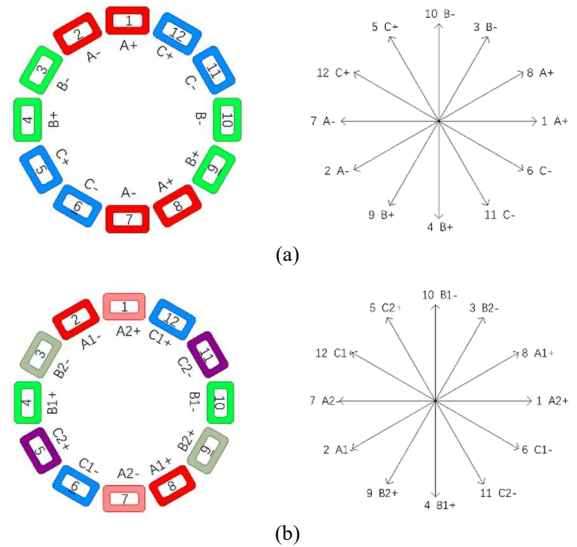

Fig. 3. Coil configuration of one stator disk: (a) W1: 3-phase short-pitch concentrated winding (b) W2: dual 3-phase full-pitch concentrated winding. (The digital indicates the number of the stator core as shown in Fig. 2)

Based on the 10 poles/12 slots combination of 3-phase AFPM, it is convenient to turn it into a novel DTP-AFPM which benefits from some additional advantages such as fault-tolerance capability, lower voltage-level and lower torque ripple. A dual 3-phase full-pitch concentrated winding is achieved by modifying the coil configuration in accordance with W2 as given in Fig. 3(b). It can be noticed that the phasor difference of two winding sets is 30 electrical degrees which eliminates the 6th harmonics in

torque ripple. The phasor arrangement of the two stator disks is shown in Fig. 4(b). The coils of the identical phase sequence are connected serially.

Besides, a more convenient method to obtain a dual 3-phase AFPM with the elimination of the coil reconfiguration and the electrical connection between two stator disks is proposed. The coil configurations of both stator disks continue to adopt W1 while the back stator is shifted by certain mechanical degrees δ as shown in Fig. 5. Then, two sets of 3-phase windings with δ_e phasor difference are obtained on the two stator disks as shown in Fig. 4(c). The shifted angle δ is set to 6 mechanical degrees (30 electrical degrees).

$$\delta_e = 5\delta \qquad (1)$$

The DTP-AFPM transformed by above two methods are named by shift model for the machine with coil configuration W1 and no shift model for the machine with coil configuration W2. For both two models, the dual 3-phase winding are connected into two separated neutral point to eliminate the influence of the zero-sequence current.
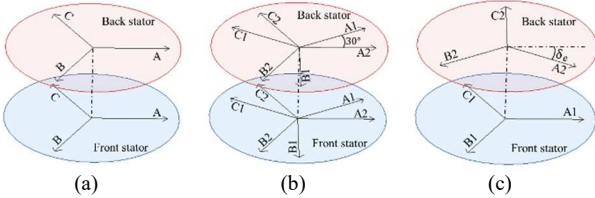

Fig. 4. Phasor arrangement diagram of the two stator disks: (a) 3-phase AFPM with W1 (b) DTP-AFPM with W2 (c) DTP-AFPM with W1.
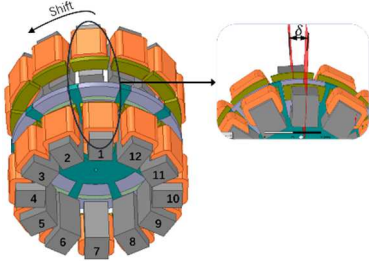

Fig. 5. Physical diagram of the stator disks with shift.

B. Comparison of the Electromagnetic Analysis Results

According to the design parameters given in [1] and the modification illustrated above, two DTP-AFPM models (shift model and no shift model) are constructed and analyzed using ANSYS MAXWELL.

The back-EMF waveforms of these two models are given in Fig. 6. The models are operated as generators and the open-circuit output phase voltages are calculated. For the shift model, the RMS of phase voltage is 79.5V. For no shift model, it is 82.4V. The harmonic component in back-EMF of the shift model and no shift model is analyzed using Fourier analysis and compared as shown in Fig. 7. The total harmonic distortion (THD) of the phase back-EMF of the shift model is 8.4% while it is 11.1% for the no shift model. It can be concluded that the no shift model is with a higher back-EMF benefiting from which it can produce higher torque under the same input current, however, its harmonic component is more significant. The

main reason of the difference on the back-EMF between these two models is that the winding factor of the no shift model is 1 that means there is no discount for the synthesis of back-EMF and no offset of the specific harmonic components. The main harmonic component in back-EMF is 3rd as shown in Fig. 7 which can be eliminated eventually due to the separated neutral points.
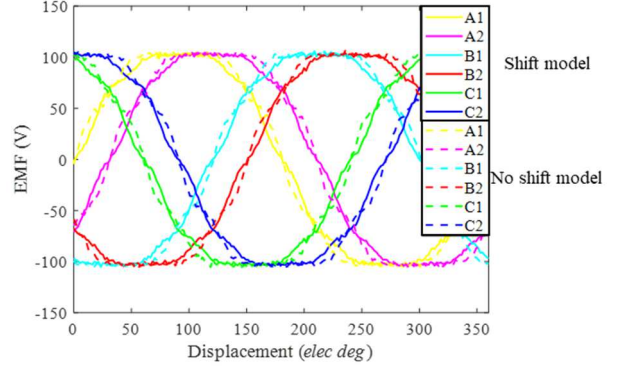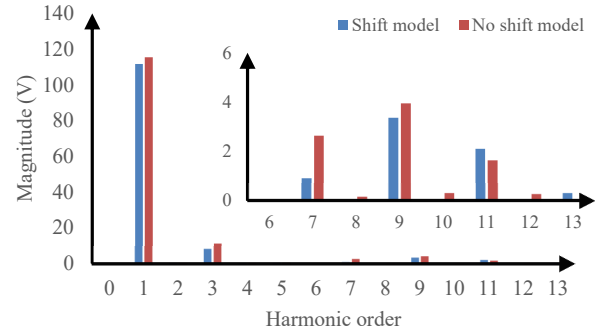

Fig. 6. Comparison of back-EMF waveforms.

Fig. 7. Comparison of the harmonic component in back-EMF.

The rated torque of DTP-AFPMs is 17.2Nm. The comparison of the percentage of the cogging torque relative to rated torque between the shift and no shift models is shown in Fig. 8. The percentage value of the shift model is while it is of the no shift model.
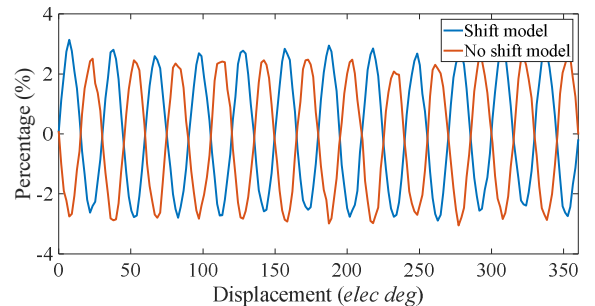

Fig. 8. The comparison of the percentage of the cogging torque relative to rated torque.

III. CONTROL OF DTP-AFPM

The control system of DTP-AFPM is shown in Fig. 9. The mathematical model of DTP-AFPM is constructed based on the vector space decomposition (VSD) method in [16]. By use of the VSD, all the variables of the machine are transformed into a decoupled frame consists of the

orthogonal *D1-Q1* axes and *D2-Q2* axes. The torque equation of DTP-AFPM under decoupled *DQ*-frame is simplified in the form of (2) and the current components on *D1*, *D2* as well as *Q2* axis are equal to 0 while the machine operates under healthy condition and the harmonics in phase current is neglected.
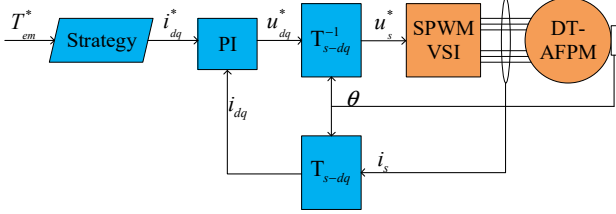

Fig. 9. The schematic diagram of the control system.

$$T_{em} = \sqrt{3}p\Psi_M i_{Q1} \qquad , (2)$$

in which the symbol p indicates the pole pairs, Ψ_M indicates the magnitude of the fundamental flux linkage.
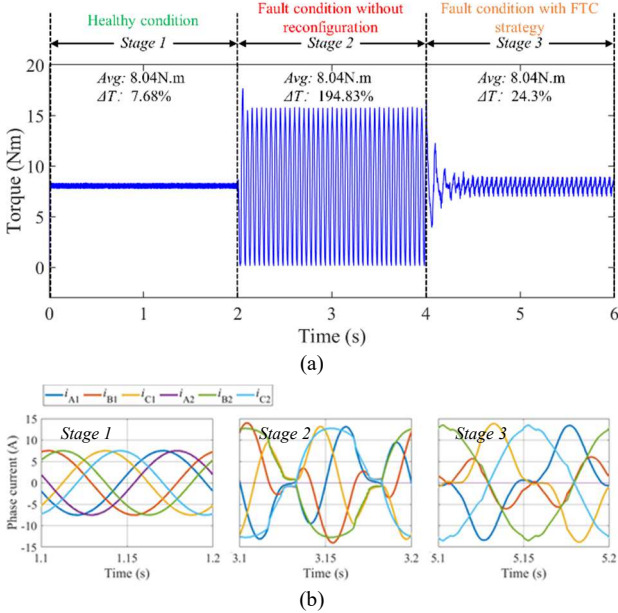

Fig. 10. Simulation results of the shift model: (a) Electromagnetic torque. (b) Phase current.

While the DTP-AFPM operates under a fault condition in which the open-circuit fault in phase A2 is assumed, the output electromagnetic torque will fluctuate greatly if the reference current is still calculated using the control strategy under healthy condition. In order to output a smooth torque under fault condition, a fault tolerant control (FTC) strategy in [17] is referenced. The reference current on DQ-frame under fault condition is reconfigured as given in (3). The factor I_F is determined by the torque equation (4).

$$\begin{cases} i_{D1,f} = \dfrac{I_F}{2}\sin(2\theta - \dfrac{\pi}{6}) \\ i_{Q1,f} = I_F \\ i_{D2,f} = I_F \cos(2\theta + \dfrac{5\pi}{6}) \\ i_{Q2,f} = \dfrac{I_F}{2}\sin(2\theta - \dfrac{\pi}{6}) \end{cases} \qquad , (3)$$

in which symbol θ indicates the rotor electrical position.

$$T_{em} = \sqrt{3}p\Psi_M i_{Q1,f} = \sqrt{3}p\Psi_M I_F \qquad (4)$$

The simulation of the DTP-AFPM consists of 3 stages:

Stage 1: The machine operates under healthy condition;

Stage 2: The phase A2 is open without reconfiguration for reference current;

Stage 3: The phase A2 is open and the reference current is calculated using FTC strategy.

In above described 3 stages, the reference torque is set to 8 Nm and the operating speed is 120 RPM. The simulated electromagnetic torque and phase current waveforms in one electrical cycle of both shift model and no shift model are given in Fig. 10 and Fig. 11, respectively.
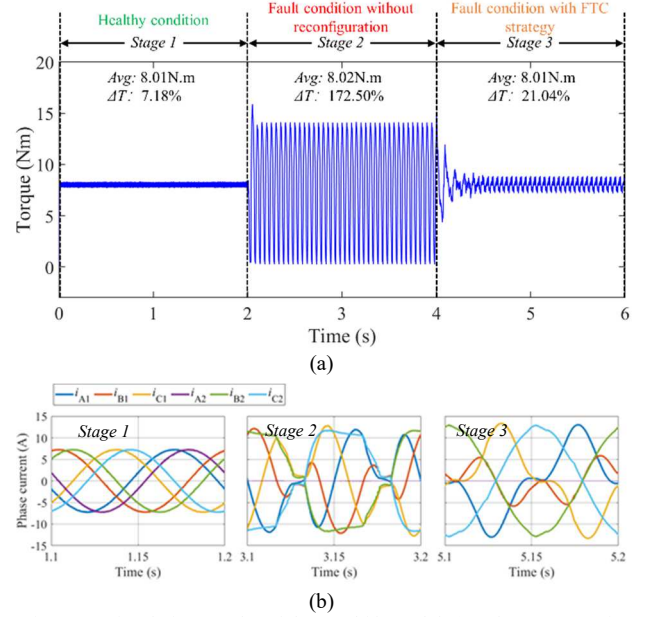

Fig. 11. Simulation results of the no shift model: (a) Electromagnetic torque. (b) Phase current.

IV. ANALYSIS OF AXIAL STRESS

As an axial flux machine characterized by the light-weight disk-type coreless rotor, DTP-AFPM is more sensitive to the axial stress. To prevent the potential possibility of unacceptable NVH (Noise, Vibration and Harshness) and mechanical damage of the machine during the operation, the axial stress on the rotor is significant to be analyzed and treated as a critical evaluation indicator for judging the feasibility of the proposed DTP-AFPM. It is clear that the axial stress on the rotor of the no shift model is balanced while it is unbalanced in the shift model due to its asymmetrical structure. In this section, the axial stress and total axial force on the rotor are calculated and compared for both shift model and no shift model.

A. Calculation Method of Synthetic axial stress

According to the Maxwell Stress Tensor (MST) principle, the normal stress on one face can be calculated by following equation:

$$f_z = \frac{1}{2\mu_0}(B_z^2 - B_x^2 - B_y^2) \qquad , (5)$$

in which the symbol μ_0 means the magnetic permeability of the air, B_x, B_y and B_z are given in Fig. 12. The symbol B_z is the normal flux density component while the B_x and B_y are a pair of the orthogonal tangential flux density component along the surface of the PM. In the case of the DTP-AFPM, the z-axis in Fig. 12 can be seen as the axial axis.
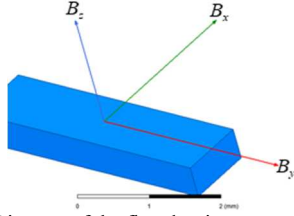

Fig. 12. Diagram of the flux density vector components.

The detailed calculating procedure of the synthetic axial stress under both healthy and fault condition is as follows:

1) Calculate the phase current of DTP-AFPM under different conditions;
2) Impose the calculated phase current as shown in Fig. 10(b) and Fig. 11(b) into the finite element analysis (FEA) model of DTP-AFPM;
3) Solve the flux density distribution in ANSYS MAXWELL, and calculate the axial stress distribution using (5);
4) Superimpose the calculated axial stress values at corresponding positions on the two sides of the rotor to get the synthetic axial stress which can be presented on a 2-D circular area as shown in Fig. 13 in which the middle lines locate at the average radius of the PMs. Furtherly, the initial circular area is unfolded to two rectangular area.
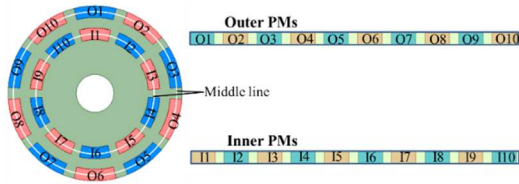

Fig. 13. Unfolding procedure from circular area to rectangular area.

B. Synthetic Axial Stress in the No Shift Model

Firstly, the rotor axial force waveform of the no shift model while the machine operates in different stages is shown in Fig. 14 in which the symbol θ_m indicates the mechanical displacement angle of the rotor. It can be seen that all the axial force waveforms fluctuate around 0 N. The synthetic axial stress distributions of the no shift model at the initial moment ($\theta_m=0$) are shown in Fig. 15. Among the six subgraphs in Fig. 15, there is no obvious regularity can be found. The peak value of each figure is indicated and the extremum is about 0.1MPa which is most likely due to the calculation errors.
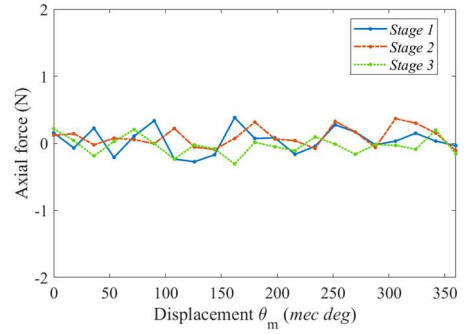

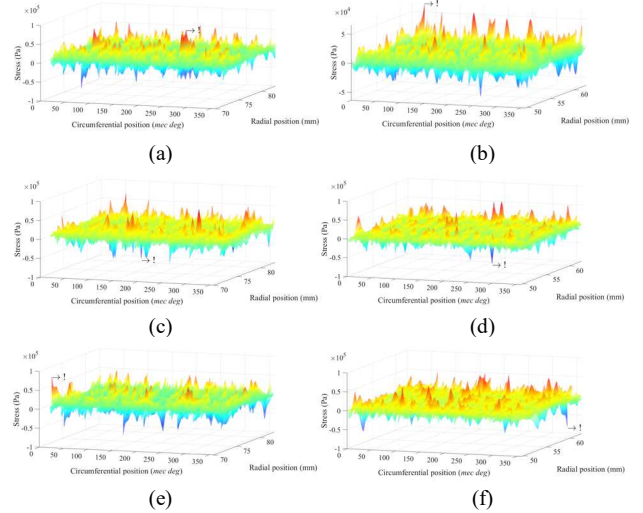Fig. 14. Rotor axial force waveform of the no shift model.

Fig. 15. Synthetic axial stress distribution of the no shift model at the initial moment: (a) on the outer PMs area operating under healthy condition, (b) on the inner PMs area operating under healthy condition, (c) on the outer PMs area operating under fault condition, (d) on the inner PMs area operating under fault condition, (e) on the outer PMs area operating under fault condition with FTC, (f) on the inner PMs area operating under fault condition with FTC.

C. Synthetic Axial Stress in the Shift Model

The rotor axial forces of the shift model while the machine operates in different stages are shown in Fig. 16. The average value of the rotor axial force in one electrical circle is -2.24N under healthy condition (*stage 1*). It means that the bearing on one side will support the axial force throughout. Under fault condition (*stage 2*), the rotor axial force deteriorates sharply that fluctuates between ± 100N. It is bound to cause the serious vibration and noise. Under fault condition with FTC (*stage 3*), the fluctuation of the rotor axial force waveform decreases clearly. However, it is still at a higher level.

In Fig. 16, a special rotor displacement position $\theta_m=294°$ is highlighted where the axial force on the rotor reaches the extremum under fault conditions (stage 2 and 3). The synthetic axial stress distribution of the shift model at $\theta_m=294°$ is shown in Fig. 17. It can be seen that the synthetic axial stress on PMs of the shift model is variable regularly along the circumferential direction. The peak value of each figure is indicated in Fig. 17. The comparison of the peak value of the axial stress between the no shift model and shift model is given in TABLE I. It can be found that the peak value of the shift model is higher than that of the no shift model. The detailed synthetic axial

stress distributions along the middle line shown in Fig. 13 are given in Fig. 18. The positive or negative fluctuation of the distribution curves shown in Fig. 18 is coincide with the position of the slot opens in stator disks. In addition, it can be noticed that the fluctuation of the axial stress on the inner PMs as shown in Fig. 18(b) is higher due to the larger slot opens and smaller flux area compared with the outer PMs. It can be predicted that the possibility of the PMs breaking increases greatly compared with the no shift model as the synthetic axial stress on each PM of the shift model is uneven.

TABLE I
COMPARISON OF THE PEAK VALUE OF THE AXIAL STRESS (UNIT: MPA)

		No shift	Shift
Healthy	Outer PM	0.0758	-0.31
	Inner PM	0.0663	-0.295
Fault	Outer PM	-0.0973	-0.377
	Inner PM	-0.0803	-0.239
FTC	Outer PM	0.0778	-0.288
	Inner PM	-0.084	-0.349

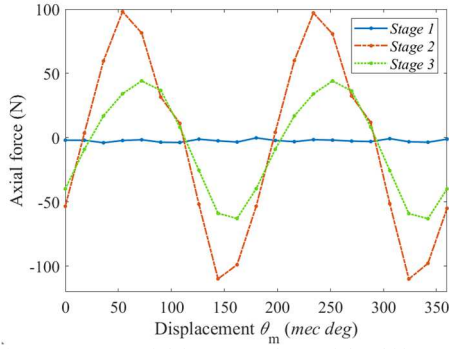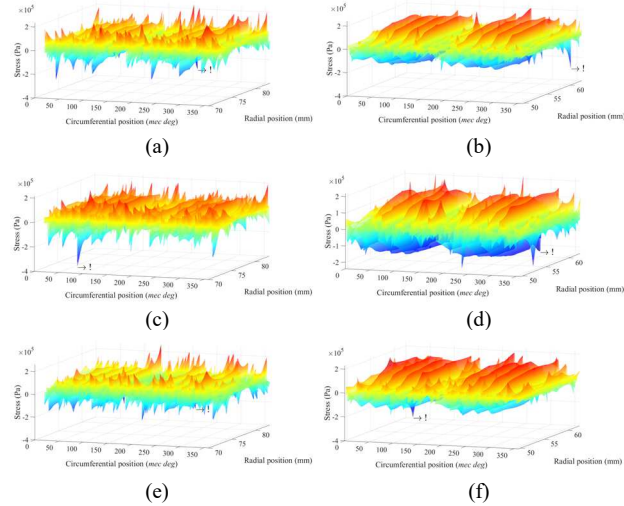
Fig. 16.   Rotor axial force waveform of the shift model.

Fig. 17.   Synthetic axial stress distribution of the shift model (θ_m=324°): (a) on the outer PMs area operating under healthy condition, (b) on the inner PMs area operating under healthy condition, (c) on the outer PMs area operating under fault condition, (d) on the inner PMs area operating under fault condition, (e) on the outer PMs area operating under fault condition with FTC, (f) on the inner PMs area operating under fault condition with FTC.
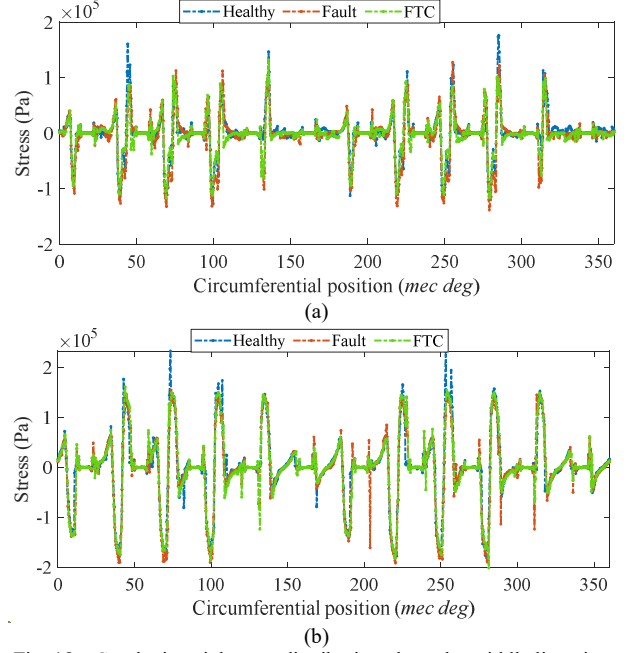

(a)

(b)

Fig. 18.   Synthetic axial stress distribution along the middle line given in Fig. 13: (a) on the outer PMs area, (b) on the inner PMs area.

V.   CONCLUSION

The DTP-AFPM is proposed in this paper including the shift model and the no shift model. The electromagnetic performances of these two models are compared. The synthetic axial stress on the rotor of the DTP-AFPM is analyzed. The main conclusions according to the investigations in this paper are summarized as follows:

1) The shift model is a more accessible structure for DTP-AFPM due to the elimination of both the electrical connection between the two stator disks and reconfiguration of the coils.

2) The no shift model is characterized by a higher back-EMF benefiting from its full-pitch winding arrangement, while its harmonics in back-EMF is degraded compared with the shift model. The cogging torques of the two models are with the same magnitude and reversed phasor.

3) The fluctuation of the total axial force on the rotor of the shift model is much higher than that of the no shift model, especially operating under the fault condition. Although the FTC strategy can greatly reduce the axial force on the rotor of the shift model, its influence on the vibration and noise still exists.

4) The breaking possibility of the PMs of the shift model is much higher according to the synthetic axial stress distribution diagram given in section VI.

5) Considering the axial stress is the crucial indicator for the mechanical safety of the proposed DTP-AFPM, the no shift model is the best choice.

REFERENCES

[1]   Zhang W, Xu Y, Zhou G. Research on a Novel Transverse Flux Permanent Magnet Motor With Hybrid Stator Core and Disk-Type Rotor for Industrial Robot Applications[J]. IEEE Transactions on Industrial Electronics, 2020, 68(11): 11223-11233.

[2] Liu Y, Niu S, Fu W N. A novel multiphase brushless power-split transmission system for wind power generation[J]. IEEE Transactions on Magnetics, 2015, 52(2): 1-7.

[3] Liu G, Yang J, Zhao W, et al. Design and analysis of a new fault-tolerant permanent-magnet vernier machine for electric vehicles[J]. IEEE Transactions on Magnetics, 2012, 48(11): 4176-4179.

[4] Levi E. Multiphase electric machines for variable-speed applications[J]. IEEE Transactions on industrial electronics, 2008, 55(5): 1893-1909.

[5] Zhang L, Fan Y, Lorenz R D, et al. Design and comparison of three-phase and five-phase FTFSCW-IPM motor open-end winding drive systems for electric vehicles applications[J]. IEEE Transactions on Vehicular Technology, 2017, 67(1): 385-396.

[6] Wang J, Qu R, Zhou L. Dual-rotor multiphase permanent magnet machine with harmonic injection to enhance torque density[J]. IEEE Transactions on Applied Superconductivity, 2011, 22(3): 5202204-5202204.

[7] Locment F, Semail E, Kestelyn X. Vectorial approach-based control of a seven-phase axial flux machine designed for fault operation[J]. IEEE Transactions on Industrial Electronics, 2008, 55(10): 3682-3691.

[8] Slunjski M, Stiscia O, Jones M, et al. General torque enhancement approach for a nine-phase surface PMSM with built-in fault tolerance[J]. IEEE Transactions on Industrial Electronics, 2020, 68(8): 6412-6423.

[9] Zhao T, Wu S, Cui S. Multiphase PMSM with asymmetric windings for more electric aircraft[J]. IEEE Transactions on Transportation Electrification, 2020, 6(4): 1592-1602.

[10] Villani M, Tursini M, Fabri G, et al. High reliability permanent magnet brushless motor drive for aircraft application[J]. IEEE transactions on industrial electronics, 2011, 59(5): 2073-2081.

[11] Shokri, Maryam, et al. "Comparison of performance characteristics of axial-flux permanent-magnet synchronous machine with different magnet shapes." IEEE Transactions on Magnetics 51.12 (2015): 1-6.

[12] Simón-Sempere, Vicente, et al. "Optimisation of Magnet Shape for Cogging Torque Reduction in Axial-Flux Permanent-Magnet Motors." IEEE Transactions on Energy Conversion 36.4 (2021): 2825-2838.

[13] Park S, Kim W, Kim S I. A numerical prediction model for vibration and noise of axial flux motors[J]. IEEE Transactions on Industrial Electronics, 2014, 61(10): 5757-5762.

[14] Deng W, Zuo S. Axial force and vibroacoustic analysis of external-rotor axial-flux motors[J]. IEEE Transactions on Industrial Electronics, 2017, 65(3): 2018-2030.

[15] Lu H, Li J, Qu R, et al. Reduction of unbalanced axial magnetic force in postfault operation of a novel six-phase double-stator axial-flux PM machine using model predictive control[J]. IEEE Transactions on Industry Applications, 2017, 53(6): 5461-5469.

[16] Kallio S, Andriollo M, Tortella A, et al. Decoupled dq model of double-star interior-permanent-magnet synchronous machines[J]. IEEE Transactions on Industrial Electronics, 2012, 60(6): 2486-2494.

[17] Feng, Guodong, et al. "Open-phase fault modeling and optimized fault-tolerant control of dual three-phase permanent magnet synchronous machines." IEEE Transactions on Power Electronics 34.11 (2019): 11116-11127.